

Vision-Based Sensor and Navigation System for Autonomous Air Refueling

John Valasek,* Kiran Gunnam,[†] Jennifer Kimmett,[‡] Monish D. Tandale,[‡] and John L. Junkins[‡]

Texas A&M University, College Station, Texas 77843-3141

and

Declan Hughes[§]

StarVision Technologies, Inc., College Station, Texas 77840

Autonomous in-flight aerial refueling is an important capability for the future deployment of unmanned aerial vehicles, because they will likely be ferried in flight to overseas theaters of operation instead of being shipped unassembled in containers. A reliable sensor, capable of providing accurate relative position measurements of sufficient bandwidth, is key to such a capability. A vision-based sensor and navigation system is introduced that enables precise and reliable probe-and-drogue autonomous aerial refueling for non-micro-sized unmanned aerial vehicles. A performance robust controller is developed and integrated with the sensor system, and feasibility of the total system is demonstrated by simulated docking maneuvers with both a stationary drogue and a drogue subjected to light turbulence. An unmanned air vehicle model is used for controller design and simulation. Results indicate that the integrated sensor and controller enables precise aerial refueling, including consideration of realistic measurement errors and disturbances.

Introduction

TWO approaches are currently used for aerial refueling. The U.S. Air Force uses the flying boom developed by Boeing. The boom approach is supervised and controlled by a human operator from a station near the rear of the tanker aircraft, who is responsible for “flying” the boom into the refueling port on the receiver aircraft. In this method, the job of the receiver aircraft is to maintain proper refueling position with respect to the tanker and leave the precision control function to the human operator in the tanker. The probe-and-drogue refueling system is the standard for the U.S. Navy and the air forces of most other nations. In this method, the tanker trails a hose with a flexible “basket,” called a drogue, at the end. The drogue is aerodynamically stabilized. It is the responsibility of the pilot of the receiver aircraft to maneuver the receiver’s probe into the drogue as shown in Figs. 1 and 2. This is the preferred method for small, agile aircraft such as fighters because both the hose and drogue are flexible and essentially passive during refueling; a human operator is not required on the tanker.^{1–3}

Autonomous in-flight refueling using a probe-and-drogue system is basically a docking situation that probably requires 2-cm accuracy in the relative position of the refueling probe (from the receiving aircraft) with respect to the drogue (from the tanker) during the end game. This specification is based on the geometry of the existing probe and drogue hardware and the need to ensure that the tip of the

probe contacts only the inner sleeve of the receptacle and not the more lightly constructed and easily damaged shroud (Bandak, M., personal conversation, Sargent Fletcher, Inc., Jan. 2002). The maturation of the technology requires several issues to be addressed, the most fundamental being the lack of sufficiently accurate/reliable relative motion sensors.⁴ Some methods that have been considered for determining relative position in a refueling scenario include the global positioning system (GPS) and visual servoing with pattern recognition software.^{5–9} GPS measurements have been made with 1- to 2-cm accuracy for formation flying, but problems associated with lock-on, integer ambiguity, and low bandwidth present challenges for application to in-flight refueling. Pattern recognition codes are not sufficiently reliable in all lighting conditions, and with adequate fault tolerance, might require large amounts of computational power to converge with sufficient confidence to a solution.^{5–7}

Another candidate is a vision-based navigation system called VisNav, which provides high-precision six-degree-of-freedom information for real-time navigation applications. VisNav is a cooperative vision technology in which a set of beacons mounted on a target body (e.g., the drogue) is supervised by a VisNav sensor mounted on a second body (e.g., the receiver aircraft). In principle, the VisNav system will work with legacy probe-and-drogue refueling systems. The only major equipment change is the addition of the VisNav sensor to the receiver aircraft. For many years drogues have been equipped with light-emitting diodes (LED) to aid human pilots with night refueling operations. VisNav can use either these existing LEDs for beacons, or ideally, infrared LEDs. This paper develops the VisNav system for the autonomous aerial refueling of aircraft. The capability of the VisNav system to accurately determine the position and attitude of the receiver aircraft in relation to a stationary drogue is demonstrated using simulation.

The paper is organized as follows. First, the basic working principles and components of the VisNav system are presented, followed by a development of the estimation of relative positions and the measurement model. This is followed by the navigation solution and derivation of the proportional-integral-filter optimal nonzero setpoint controller with control rate weighting (PIF-NZSP-CRW). Detailed software models of the VisNav system are then integrated with the PIF-NZSP-CRW controller and evaluated with docking maneuvers on a six-degree-of-freedom simulation of an unmanned air vehicle (UAV). Finally, the Dryden gust model with light turbulence is used to assess controller performance and disturbance accommodation characteristics in the presence of exogenous inputs.

Presented as Paper 2002-3441 at the AIAA 1st Unmanned Aerospace Vehicles, Systems, Technologies, and Operations Conference, Portsmouth, VA, 22–24 May 2002; received 1 July 2004; revision received 11 November 2004; accepted for publication 11 November 2004. Copyright © 2004 by John Valasek. Published by the American Institute of Aeronautics and Astronautics, Inc., with permission. Copies of this paper may be made for personal or internal use, on condition that the copier pay the \$10.00 per-copy fee to the Copyright Clearance Center, Inc., 222 Rosewood Drive, Danvers, MA 01923; include the code 0731-5090/05 \$10.00 in correspondence with the CCC.

*Associate Professor and Director, Flight Simulation Laboratory, Aerospace Engineering Department, 3141 TAMU; valasek@aero.tamu.edu. Associate Fellow AIAA.

[†]Graduate Research Assistant, Aerospace Engineering Department, 3141 TAMU. Student Member AIAA.

[‡]Distinguished Professor, George J. Eppright Chair, and Director, Center for Mechanics and Control, 3141 TAMU, Aerospace Engineering Department; junkins@tamu.edu. Fellow AIAA.

[§]Chief Engineer; dhughes@starvisiontech.com.

Vision-Based Navigation Sensor and System

The VisNav sensor comprises an optical sensor combined with structured active light sources (beacons) to achieve a selective or “intelligent” vision. VisNav structures the light in the frequency domain, analogous to radar, so that discrimination and target identification are near trivial even in a noisy ambient environment. This is accomplished by fixing several LED-based beacons to the target frame A and an optical sensor, based on a position-sensing diode (PSD), to the sensor frame B. The LEDs emit structured light modulated with a known waveform, which permits filtering of the received beacon energy so that most of the much larger ambient energy can be rejected. To address the depth of field problem commonly associated with optical sensors, the power of each LED beacon is adaptively adjusted online to optimize the received energy amplitude. This maximizes the signal-to-noise ratio of each individual measurement and is accomplished by a wireless feedback loop closed at 100 Hz.

For application to the endgame docking problem of autonomous aerial refueling of aircraft, consider a VisNav sensor (a PSD) mounted on a receiver aircraft and a set of LED beacons mounted on a drogue being trailed from a tanker aircraft (Fig. 3). When light energy from an individual beacon on the drogue is focused on the surface of the PSD, it generates electrical current, which is measured with four pickoff leads, one on each side. The closer the image centroid is to a given pickoff lead, the stronger the current is through that lead. From the current imbalance in the two horizontal leads, the horizontal displacement of the light centroid can be estimated. Similarly, the current imbalance in the vertical leads provide an estimate of the vertical displacement of the image centroid.

In reality, a weak cross-channel coupling and other nonlinearities are present. These are handled with a nonlinear mapping determined in a one-time calibration that linearizes this relationship. The calibration functions are then applied in real time. The horizontal and vertical image centroid displacement measurements vary in a monotonic relationship with the azimuth and elevation of the beacon source, with respect to the local sensor frame. When these data are collected for four or more separate beacons, the navigation solution is calculated with a Gaussian least-squares differential-correction

(GLSDC) routine. The solution consists of six-degree-of-freedom sensor position and attitude data with respect to the target frame A and is provided at an update rate of 100 Hz (Refs. 10–12). For the aerial refueling application, Fig. 4 shows a conceptual installation of VisNav LED beacons on the drogue basket. The infrared VisNav beacons would be attached at the same locations on the drogue currently occupied by visible LED navigation lights.

The basic architecture of the VisNav system is shown in Fig. 5. The sensor digital signal processor (DSP) on the receiver UAV selects a beacon from the available set and transmits the beacon number and desired intensity via an infrared digital optical link to the beacon controller located on the drogue. The beacon controller responds by turning on the beacon selected by the sensor, at the requested intensity. The PSD (lower right-hand corner of the sensor block) generates four electrical currents—left (L), right (R), up (U),

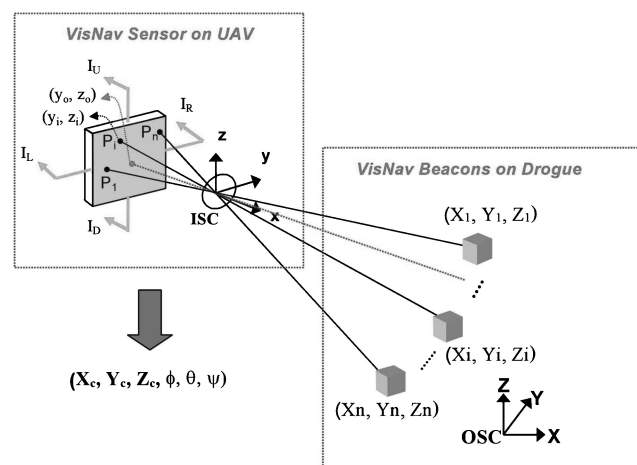


Fig. 3 Illustration of VisNav system and geometries.



Fig. 1 AV-8B Harrier refueling using the probe-and-drogue method.



Fig. 4 Conceptual VisNav LED beacon configuration on drogue basket.

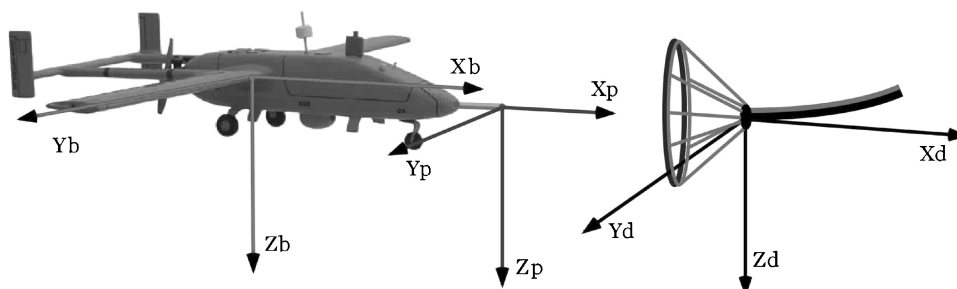


Fig. 2 Geometry and axis conventions for the probe-and-drogue refueling problem.

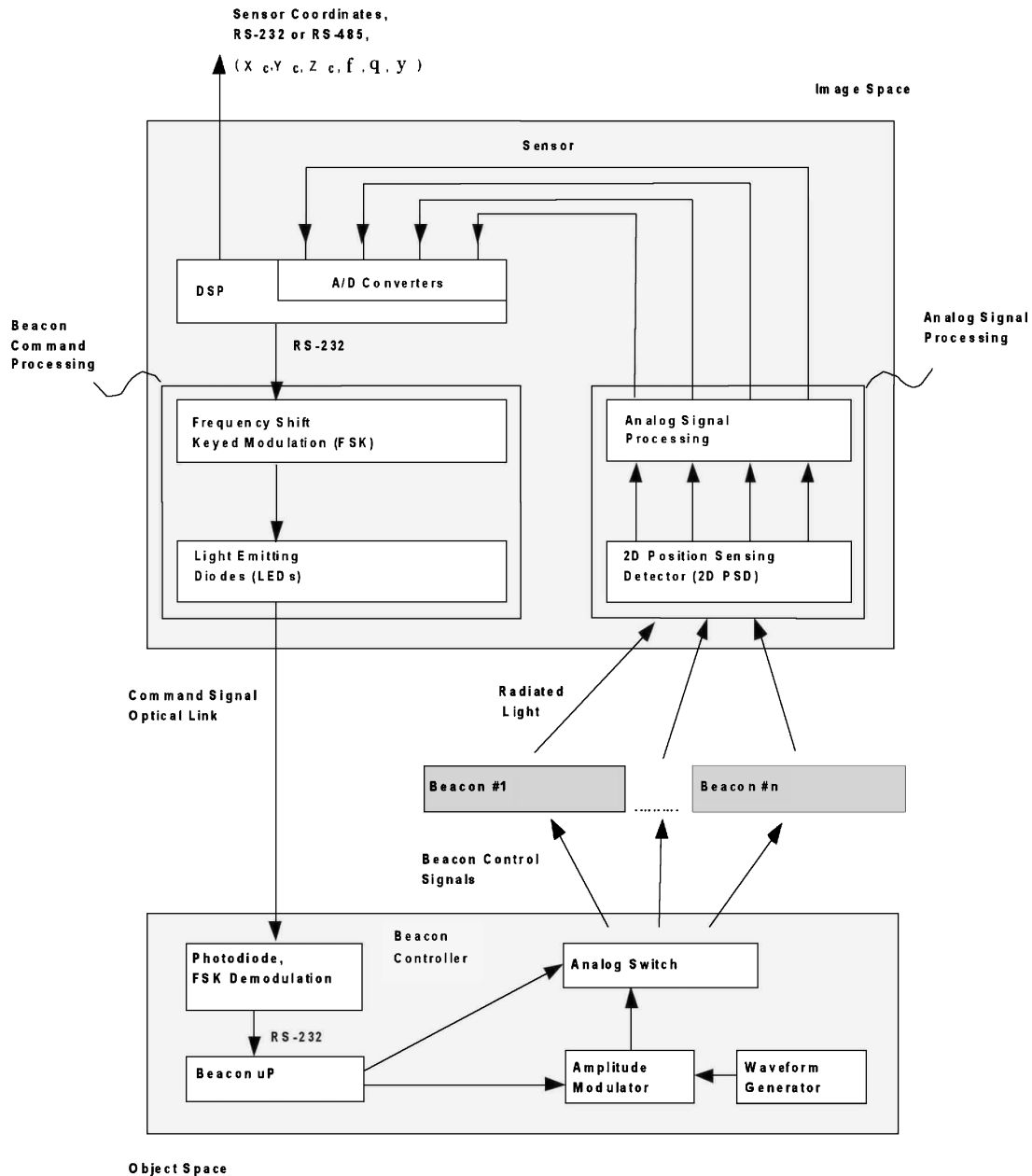


Fig. 5 VisNav system architecture.

and down (D)—in response to the infrared (IR) light image of this beacon. The four currents contain a carrier frequency to provide discrimination against sunlight, engine energy, etc., and must be amplified and demodulated before conversion to digital form for the DSP CPU. After the DSP has selected at least four distinct beacons in sequence, and the four PSD signals have been collected for each, the algorithm can compute the six-degree-of-freedom position and attitude of the sensor aircraft with respect to the drogue, in the drogue frame of reference, and viceversa. The use of frequency structured light and subsequent filtering in the sensor permit the VisNav system to be used in a wide variety of lighting conditions likely to be encountered during aerial refueling operations. Specifically, the PSD preamplifier is able to operate in the presence of sunlight, which is orders of magnitude larger than the beacon signal, close to the associated shot-noise limit. The beacons emit light modulated at 40 KHz, and the sensor filters out all light except that which lies close to 40 KHz. This frequency was chosen as a compromise between avoiding lower-frequency energy from natural and artificial light sources and avoiding increased sensor amplifier noise effects at higher frequencies. Furthermore, a colored-glass optical filter is placed outside the sensor lens to block out virtually all visible light

(including about 95% of the solar energy) while passing the IR wavelengths produced by the beacons. This passive filter greatly reduces random shot noise, which is proportional to the square root of all energy incident on the detector. The near IR wavelength of 880 nm is chosen to lie close to the optimal response wavelength of the silicon PSD.^{10–12} Although the PSD sensitivity is broad enough that beacons in the visible range with most any color could be used, more power would have to be broadcast as a result of decreased PSD sensitivity in that range.

Performance of the VisNav system is a strong function of beacon intensity. If the power output from a particular beacon is too high, one or more of the PSD transimpedance amplifiers can saturate, which leads to inaccurate calculations of the light image centroid coordinates. If the energy is too low, then a poor signal-to-noise ratio is achieved. To address these issues, feedback control is used to maintain a near-constant beacon light output intensity of approximately 70% full-scale response at the output of the sensor amplifiers. This is a one-step algorithm where knowledge of the beacon intensity and sensor response level at the previous activation allows calculation of the required beacon intensity to bring the response to 70%, assuming no change in the relative positions of the beacons and sensor. In

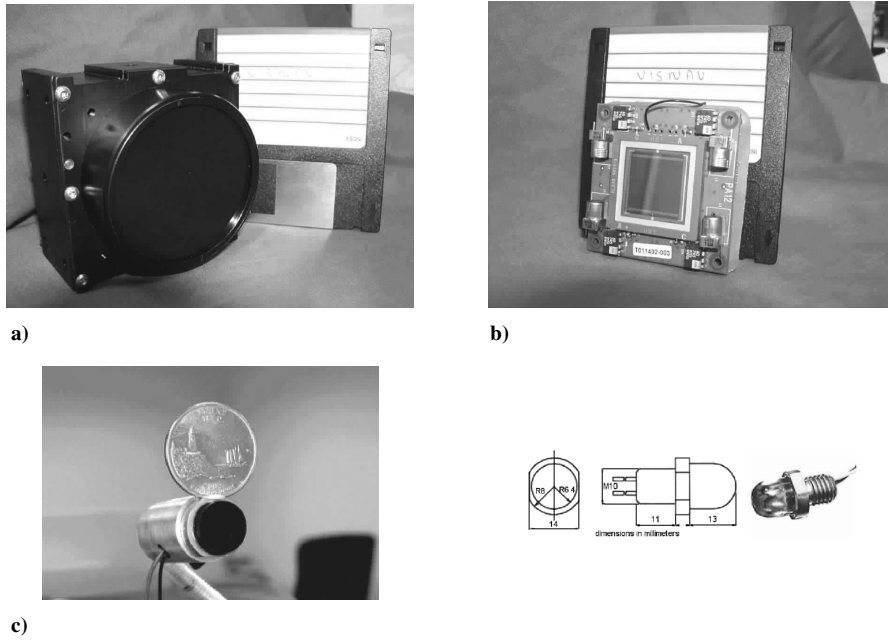


Fig. 6 VisNav system hardware components: a) sensor box, b) position-sensing-diode sensor with preamplifiers, and c) LED beacon.

practice relative movement, slight unmeasured nonlinearities, and noise/disturbances prevent perfect compensation. The beacon intensity information is conveyed from the sensor to the beacons via an IR optical or radio signal.^{10–12}

The accuracy of VisNav depends on beacon geometry. Because the accuracy is about 1:2000, accuracy in beacon positioning better than this will be in the noise level. If the beacon are 1 m apart, beacon errors smaller than 1 mm will not be an issue, and this in fact is the goal. In practice, this can be easily achieved on a rigid structure. However, on a flexible drogue it might be impossible, and this aspect is still being researched. Regarding the sensor, VisNav uses linear PSDs with very small measurement errors; less than 1:10 A Chebyshev calibration routine compensates for such errors, and the resulting errors are less than 1:5000 (single sigma standard deviation) at the calibration data points; they are at least less than 1:2500 elsewhere. This can lead to attitude errors of the order of 0.1 deg (yaw, pitch, 90 deg/2500), with better accuracies toward the center of the field of view, and lesser accuracies toward the edges. Corresponding sensor horizontal and vertical errors would be of the order of 1 mm at 1-m range and 1 cm at 10-m range.

The VisNav system is currently at the laboratory hardware stage, and several generations of prototypes have been built and successfully tested. Figure 6 shows a version 3.2 VisNav sensor box, a PSD sensor, and part of the preamplifiers. The version 4.0 VisNav sensor will have less than one-third of the volume of the version 3.2 article shown and is currently under development. The VisNav Laboratory website contains additional details and hardware descriptions.[¶]

Estimation of Relative Positions

In this subsection, i denotes the target beacon number. The four PSD imbalance current responses (left, right, up, and down) caused by the i th beacon are processed with analog circuitry (Figs. 3 and 5). The currents obtained after the process of demodulation, sampling, and analog to digital conversion are denoted $I_{R,i}$, $I_{L,i}$, $I_{U,i}$, and $I_{D,i}$. Further details on analog signal processing are provided in Ref. 10. These currents, which are in numeric form, are fed to the DSP processor for the six-degree-of-freedom solution using the algorithm described in the following discussion. The normalized voltages are computed from the PSD imbalance currents, which are proportional to azimuth and elevation of the i th beacon with respect to the image coordinate frame. These are denoted $V_{y,i}$ and $V_{z,i}$, respectively. The

normalized voltages are defined as¹¹

$$V_{y,i} = K \frac{I_{R,i} - I_{L,i}}{I_{R,i} + I_{L,i}}, \quad V_{z,i} = K \frac{I_{U,i} - I_{D,i}}{I_{U,i} + I_{D,i}} \quad (1)$$

where K is a constant of value 1. $V_{y,i}$ corresponds to the angle that the incident light beam from the i th beacon makes about the image space y axis. Similarly, $V_{z,i}$ corresponds to the angle that the incident light beam from the i th beacon makes about the image space z axis.

These normalized voltages must be mapped to the horizontal and vertical displacement estimates of that target beacon's image spot (image centroid estimates) with respect to the sensor frame. These horizontal and vertical displacement estimates are denoted \hat{y}_i and \hat{z}_i , respectively. The mapping compensates primarily for lens-induced distortion and can employ Chebyshev polynomials or some other calibration functions to compensate for these distortions. The calibration process maps the measured voltages ($V_{y,i}$, $V_{z,i}$) into (y_i, z_i) consistent with the known camera position, known object space beacon location, and the colinearity equations (pinhole camera model). Thus, the calibration function compensates for all systematic nonideal effects.

To obtain the six-degree-of-freedom solution, that is, position and attitude data, four or more beacon image centroid estimates are needed. In the following discussion, y_i , z_i are the ideal image spot centroid coordinates in the image space coordinate frame for the i th target light source; X_i , Y_i , Z_i are the known object space coordinates of the target light source (i th beacon); X_c , Y_c , and Z_c are the object space coordinates of the sensor origin attached to the lens center fixed in the vehicle; C is the direction cosine matrix of the image space coordinate frame with respect to the object space coordinate frame; F_y , F_z are the lens calibration maps; and f is the focal length of the sensor lens. The sensor electronics, the ambient light sources, and the inherent properties of the sensor produce noise in the PSD measurements. To a good approximation, this noise can be modeled as zero mean Gaussian noise. The observed measurement model \hat{h}_i is

$$\hat{h}_i = \bar{h}_i + v_i \quad (2)$$

where $\bar{h}_i(x)$ is an ideal measurement model for the i th beacon and is given by the unit vector

$$\bar{h}_i = \{y_i, z_i\}^T \quad (3)$$

and v_i is Gaussian measurement noise with covariance $R_{i,i} = E\{v_i, v_i^T\}$. Alternate choices for the measured vectors are presented.

[¶]Data available online at <http://jungfrau.tamu.edu/html/VisionLab/>.

The vector $\hat{\mathbf{h}}_i$ is the estimated measurement model for the i th beacon in the process of six-degree-of-freedom estimation and will be computed by colinearity equations. The matrices \mathbf{b} and $\hat{\mathbf{b}}$ are the observed (by the sensor) and the estimated (by the estimation algorithm) measurement models for system configuration of N beacons, respectively. N is chosen to be greater than or equal to four for good geometric triangulation of the sensor¹¹:

$$\mathbf{b} = [\mathbf{h}_1 \quad \mathbf{h}_2 \quad \cdots \quad \mathbf{h}_3]^T, \quad \hat{\mathbf{b}} = [\hat{\mathbf{h}}_1 \quad \hat{\mathbf{h}}_2 \quad \cdots \quad \hat{\mathbf{h}}_3]^T \quad (4)$$

Here $\mathbf{x} = [\mathbf{L} \quad \mathbf{p}]^T$ is the state vector of the sensor, $\mathbf{L} = [X_c \quad Y_c \quad Z_c]^T$ is the position vector, and $\mathbf{p} = [p_1 \quad p_2 \quad p_3]^T$ is the orientation/attitude vector, expressed in terms of modified Rodrigues parameters (MRP).¹³ The MRPs are defined as $\mathbf{p} = \mathbf{e} \tanh(\Phi/4)$, where $\mathbf{e} = [e_1 \quad e_2 \quad e_3]^T$ is the principal rotation axis (eigenvector of \mathbf{C} corresponding to the eigenvalue +1) and Φ is the principal rotation angle. The use of a GLSDC algorithm to determine the states, attitude, and position gives a best geometric solution in the least-square sense upon convergence through iterations.¹¹ Estimates for position and attitude are refined through iterations of GLSDC as it minimizes the weighted sum of squares

$$J = \frac{1}{2}(\mathbf{b} - \hat{\mathbf{b}})^T \mathbf{W}(\mathbf{b} - \hat{\mathbf{b}}) \quad (5)$$

where $\mathbf{W} = \mathbf{W}^T > 0$ is the weighting matrix whose entries are the covariance of the measurement noise vectors of the i th and j th beacons defined in terms of $\mathbf{R}_{i,j} = E\{\mathbf{v}_i \mathbf{v}_j^T\}$ as

$$\mathbf{W} = \begin{bmatrix} \mathbf{R}_{1,1} & \mathbf{R}_{1,2} & \cdots & \mathbf{R}_{1,N} \\ \mathbf{R}_{2,1} & \mathbf{R}_{2,2} & \cdots & \mathbf{R}_{2,N} \\ \cdots & \cdots & \cdots & \cdots \\ \mathbf{R}_{N,1} & \mathbf{R}_{N,2} & \cdots & \mathbf{R}_{N,N} \end{bmatrix}^{-1} \quad (6)$$

The ideal geometric projection from output to image space is the pinhole camera model. The pinhole camera model is based on the idealization that the object space point $P(X, Y, Z)$, the camera perspective center X_c, Y_c, Z_c , and the image point lie in a straight line. This leads to

$$\begin{pmatrix} -f \\ y_i \\ z_i \end{pmatrix} = \alpha [\mathbf{C}] \begin{Bmatrix} X_i - X_c \\ Y_i - Y_c \\ Z_i - Z_c \end{Bmatrix} \quad (7)$$

or

$$-f = \alpha [C_{11}(X_i - X_c) + C_{12}(Y_i - Y_c) + C_{13}(Z_i - Z_c)] \quad (8)$$

$$y_i = \alpha [C_{21}(X_i - X_c) + C_{22}(Y_i - Y_c) + C_{23}(Z_i - Z_c)] \quad (9)$$

$$z_i = \alpha [C_{31}(X_i - X_c) + C_{32}(Y_i - Y_c) + C_{33}(Z_i - Z_c)] \quad (10)$$

Eliminating the scale factor α from Eq. (8) and substituting into Eqs. (9) and (10) results in

$$\alpha = \sqrt{\frac{f^2 + y_i^2 + z_i^2}{(X_i - X_c)^2 + (Y_i - Y_c)^2 + (Z_i - Z_c)^2}}$$

$$\begin{aligned} y_i &= g_{yi}(X_i, Y_i, Z_i, X_c, Y_c, Z_c, C) \\ &= -f \frac{C_{21}(X_i - X_c) + C_{22}(Y_i - Y_c) + C_{23}(Z_i - Z_c)}{C_{11}(X_i - X_c) + C_{12}(Y_i - Y_c) + C_{13}(Z_i - Z_c)} \end{aligned} \quad (11)$$

$$\begin{aligned} z_i &= g_{zi}(X_i, Y_i, Z_i, X_c, Y_c, Z_c, C) \\ &= -f \frac{C_{31}(X_i - X_c) + C_{32}(Y_i - Y_c) + C_{33}(Z_i - Z_c)}{C_{11}(X_i - X_c) + C_{12}(Y_i - Y_c) + C_{13}(Z_i - Z_c)} \end{aligned} \quad (12)$$

with α being unity. An alternate vector representation for the preceding colinearity equations can be written in the unit line-of-sight vector projection¹³

$$\hat{\mathbf{h}}_i = \hat{\mathbf{C}} \mathbf{r}_i \quad (13)$$

where

$$\hat{\mathbf{h}}_i = (1/\sqrt{f^2 + y_i^2 + z_i^2}) \cdot [-f \quad y_i \quad z_i]^T$$

are the sensor frame unit vectors' $\mathbf{r}_i = (1/d_i)$,

$$[(X_i - X_c) \quad (Y_i - Y_c) \quad (Z_i - Z_c)]^T$$

are the object frame unit vectors, and

$$d_i = \sqrt{(X_i - X_c)^2 + (Y_i - Y_c)^2 + (Z_i - Z_c)^2}$$

MRPs are derived from the quaternions and yield better results in terms of linearity because they linearize like quarter-angles instead of half-angles for the quaternions.¹³ The direction cosine matrix in terms of modified Rodrigues parameters is

$$\mathbf{C} = \mathbf{I}_{3 \times 3} + \frac{8(\mathbf{p} \times)^2 - 4(\mathbf{I} - \mathbf{p}^T \mathbf{p})(\mathbf{p} \times)}{(1 + \mathbf{p}^T \mathbf{p})^2} \quad (14)$$

with

$$\mathbf{p} \times = \begin{bmatrix} 0 & -p_3 & p_2 \\ p_3 & 0 & -p_1 \\ -p_2 & p_1 & 0 \end{bmatrix} \quad (15)$$

Measurement Model

A measurement model based on normalized parameters in Eq. (13) can be used, but because f is constant there is no need to consider this parameter, and redundancy is eliminated. The measurement model used here has only two parameters but normalizes them to further linearize the GLSDC model and therefore improve convergence performance¹⁴:

$$\mathbf{h}_i = (1/\sqrt{f^2 + y_i^2 + z_i^2})[y_i \quad z_i]^T \quad (16)$$

This can be represented as

$$\mathbf{h}_i = \mathbf{D} \cdot \mathbf{r}_i \quad (17)$$

where \mathbf{D} is a 2×3 matrix whose entries are obtained from the direction cosine matrix \mathbf{C} and $D_{j,k} = C_{j+1,k}$, $j = 1, 2$; $k = 1, 2, 3$, where j and k denote the rows and the columns, respectively. The measurement sensitivity matrix for the i th beacon \mathbf{H}_i is obtained by partial differentiation of the measurement model with respect to the state vector \mathbf{x} :

$$\mathbf{H}_i = \frac{\partial \mathbf{h}_i}{\partial \mathbf{x}} = \left(\frac{\partial \mathbf{h}_i}{\partial \mathbf{L}} \quad \frac{\partial \mathbf{h}_i}{\partial \mathbf{p}} \right) \quad (18)$$

$$\frac{\partial \mathbf{h}_i}{\partial \mathbf{L}} = -\frac{\mathbf{D}\{\mathbf{I}_{3 \times 3} - \mathbf{r}_i \mathbf{r}_i^T\}}{d_i} \quad (19)$$

$$\frac{\partial \mathbf{h}_i}{\partial \mathbf{p}} = \frac{4}{(1 + \mathbf{p}^T \mathbf{p})^2} \mathbf{S}\{(1 - \mathbf{p}^T \mathbf{p})\mathbf{I}_{3 \times 3} - 2[\mathbf{p} \times] + 2\mathbf{p} \mathbf{p}^T\} \quad (20)$$

with

$$\mathbf{S} = \begin{bmatrix} s_3 & 0 & -s_1 \\ -s_2 & s_1 & 0 \end{bmatrix}, \quad \mathbf{S} \mathbf{v} = [s_1 \quad s_2 \quad s_3]^T = \mathbf{C} \cdot \mathbf{r}_i$$

The measurement sensitivity matrix is

$$\mathbf{H} = [\mathbf{H}_1^T \quad \mathbf{H}_2^T \cdots \mathbf{H}_N^T]^T \quad (21)$$

Now the measurement sensitivity matrix \mathbf{H} in Eq. (21) is $2N \times 6$ instead of $3N \times 6$, where N is the number of beacons and the weighting matrix \mathbf{W} in Eq. (6) is $2N \times 2N$ instead of $3N \times 3N$. This results in computational savings and reduced implementation complexity. Whereas the observed measurement matrix for N beacons is given by \mathbf{h}_i in Eq. (16), the estimated measurement matrix $\hat{\mathbf{b}}$ is computed using estimated position and orientation in the colinearity Eq. (13).

We mention that a sensor calibration is required to account for lens distortion, detection nonlinearity, and departures of the actual sensor behavior from the ideal pinhole camera model implicit in the preceding formulas. This calibration process operates on the sensor output to map the measurements to offset values that are adequately modeled by the colinearity equations.

GLSDC Algorithm

The algorithm operates as follows. Indices k and m correspond to time step in the flight trajectory and GLSDC algorithm iteration for measurements collected at each time step, respectively. The initial state estimate before iteration is $\hat{\mathbf{x}}_{k,0} = \hat{\mathbf{x}}_{k-1}$. If $k = 0$, the estimate $\hat{\mathbf{x}}_{k,0}$ is used. Iterations are then performed using the standard GLSDC procedure given by Eqs. (22), where $\mathbf{P}_{k,m}$ is the covariance and $\mathbf{H}_{k,m} = \mathbf{H}$ in Eq. (21) at the m th iteration at the k th time step; $\mathbf{W}_k = \mathbf{W}$ in Eq. (6), $\mathbf{b}_k = \mathbf{b}$ in Eq. (4) at the k th time step; and $\tilde{\mathbf{b}}_k$ in Eq. (4) at the m th iteration at the k th time step:

$$\begin{aligned} \mathbf{P}_{k,i} &= (\mathbf{H}_{k,i}^T \mathbf{W}_k \mathbf{H}_{k,i})^{-1}, & \Delta \hat{\mathbf{x}}_{k,i} &= \mathbf{P}_{k,i} \mathbf{H}_{k,i}^T \mathbf{W}_k (\mathbf{b}_k - \tilde{\mathbf{b}}_k, i) \\ \hat{\mathbf{x}}_{k,i+1} &= \hat{\mathbf{x}}_{k,i} + \Delta \hat{\mathbf{x}}_{k,i} \end{aligned} \quad (22)$$

Iterations stop when either 1) the states are no longer improved by the iteration or 2) the number of iterations reaches the allowable limit. This GLSDC algorithm is robust when there are four or more beacons measured, except near certain geometric conditions that are avoided by careful beacon placement and limiting the range of operation.

Optimal Nonzero Setpoint Controller

The optimal nonzero setpoint (NZSP) is a command structure that steers the plant to a terminal steady-state condition, with guaranteed tracking properties. It is used here to develop a simple yet functional baseline autonomous controller for evaluating the VisNav system in aerial refueling.¹⁴ For a linear time-invariant system with n states and m controls,

$$\begin{aligned} \dot{\mathbf{x}} &= \mathbf{A}\mathbf{x} + \mathbf{B}\mathbf{u}, & \mathbf{x}(0) &= \mathbf{x}_0, & \mathbf{y} &= \mathbf{C}\mathbf{x} + \mathbf{D}\mathbf{u} \\ \mathbf{x} &\in \mathbb{R}^n, & \mathbf{u} &\in \mathbb{R}^m, & \mathbf{y} &\in \mathbb{R}^m \end{aligned} \quad (23)$$

It is desired to command some of the initial outputs \mathbf{y} to steady-state terminal output values \mathbf{y}_m and keep them there as $t \rightarrow \infty$. If these terminal outputs are trim states, denoted by $*$, then at the terminal steady-state condition the system is characterized by

$$\begin{aligned} \dot{\mathbf{x}}^* &= \mathbf{A}\mathbf{x}^* + \mathbf{B}\mathbf{u}^* \equiv 0, & \mathbf{y}_m &= \mathbf{H}\mathbf{x}^* + \mathbf{D}\mathbf{u}^* \\ \mathbf{x}^* &\in \mathbb{R}^n, & \mathbf{u}^* &\in \mathbb{R}^m, & \mathbf{y}_m &\in \mathbb{R}^m \end{aligned} \quad (24)$$

For guaranteed tracking, the number of commanded outputs \mathbf{y}_m must be less than or equal to the number of controls m . Error states and error controls are defined as

$$\tilde{\mathbf{x}} = \mathbf{x} - \mathbf{x}^*, \quad \tilde{\mathbf{u}} = \mathbf{u} - \mathbf{u}^* \quad (25)$$

where $\tilde{\mathbf{x}}$ and $\tilde{\mathbf{u}}$ are the error between the current state and control, respectively, and the desired state and control, respectively. The state equations can be written in terms of these error states as

$$\dot{\tilde{\mathbf{x}}} = \dot{\mathbf{x}} - \dot{\mathbf{x}}^* = \mathbf{A}\mathbf{x} + \mathbf{B}\mathbf{u} - (\mathbf{A}\mathbf{x}^* + \mathbf{B}\mathbf{u}^*), \quad \dot{\tilde{\mathbf{x}}} = \mathbf{A}\tilde{\mathbf{x}} + \mathbf{B}\tilde{\mathbf{u}} \quad (26)$$

with quadratic cost function to be minimized:

$$J = \frac{1}{2} \int_0^\infty (\tilde{\mathbf{x}}^T \mathbf{Q} \tilde{\mathbf{x}} + \tilde{\mathbf{u}}^T \mathbf{R} \tilde{\mathbf{u}}) dt \quad (27)$$

The optimal control, which minimizes Eq. (27), is obtained by solving the matrix algebraic Riccati equation for infinite horizon:

$$\mathbf{P}\mathbf{A} + \mathbf{A}^T \mathbf{P} - \mathbf{P}\mathbf{B}\mathbf{R}^{-1} \mathbf{B}^T \mathbf{P} + \mathbf{Q} = 0 \quad (28)$$

resulting in

$$\mathbf{P}\mathbf{A} + \mathbf{A}^T \mathbf{P} - \mathbf{P}\mathbf{B}\mathbf{R}^{-1} \mathbf{B}^T \mathbf{P} + \mathbf{Q} = 0 \quad (29)$$

A feedback control law in terms of the measured states is obtained by converting $\tilde{\mathbf{u}}$ back to \mathbf{u} , giving

$$\mathbf{u} = (\mathbf{u}^* + \mathbf{K}\mathbf{x}^*) - \mathbf{K}\mathbf{x} \quad (30)$$

with \mathbf{u}^* and \mathbf{x}^* constants. They are solved for directly by inverting a quad partition matrix deduced from Eq. (24):

$$\begin{bmatrix} \mathbf{A} & \mathbf{B} \\ \mathbf{H} & \mathbf{D} \end{bmatrix}^{-1} = \begin{bmatrix} \mathbf{X}_{11} & \mathbf{X}_{12} \\ \mathbf{X}_{21} & \mathbf{X}_{22} \end{bmatrix}, \quad \begin{bmatrix} \mathbf{x}^* \\ \mathbf{u}^* \end{bmatrix} = \begin{bmatrix} \mathbf{X}_{11} & \mathbf{X}_{12} \\ \mathbf{X}_{21} & \mathbf{X}_{22} \end{bmatrix} \begin{bmatrix} \mathbf{0} \\ \mathbf{y}_m \end{bmatrix} \quad (31)$$

and then solving for

$$\mathbf{x}^* = \mathbf{X}_{12} \mathbf{y}_m, \quad \mathbf{u}^* = \mathbf{X}_{22} \mathbf{y}_m \quad (32)$$

Upon substitution in Eq. (30), the control law implementation equation becomes

$$\mathbf{u} = (\mathbf{X}_{22} + \mathbf{K}\mathbf{X}_{12}) \mathbf{y}_m - \mathbf{K}\mathbf{x} \quad (33)$$

For the optimal control policy \mathbf{u} to be admissible, the quad partition matrix must be invertible. Therefore, the equations for \mathbf{x}^* and \mathbf{u}^* must be linearly independent, and the number of outputs or states that can be driven to a constant value must be less than or equal to the number of available controls. An advantage of this controller is the guarantee of perfect tracking of a number of outputs equal to the number of controls, independent of the value of the gains, provided they are stabilizing. The gains can be designed using any desired technique and only affect the transient performance, and not the guarantee of steady-state performance.

Proportional Integral Filter with Control Rate Weighting

The optimal NZSP controller just developed assumes that there are no exogenous inputs to the system. A controller for autonomous aerial refueling must possess both stability robustness and performance robustness because it must operate in the presence of uncertainties, particularly unstructured uncertainties such as atmospheric turbulence. One technique to improve disturbance accommodation properties of a controller to exogenous inputs is to prefilter the control commands with a low-pass filter. This will also reduce the risk of pilot-induced oscillations by reducing control rates. An effective technique that permits the performance of the prefilter to be tuned with quadratic weights, called optimal control rate weighting, is used for this purpose. It is developed here as part of the broader proportional-integral-filter (PIF) methodology, as an extension of the optimal NZSP. The resulting controller is termed PIF-NZSP-CRW and is shown in Fig. 7. A type-1 system performance is desired, and so integrator states \mathbf{y}_I are created such that body-axis velocities u and v are integrated to x_{body} and y_{body} . To obtain the desired filtering of the controls, the rates of the controls are also added as states \mathbf{u}_I . The optimal NZSP is extended into the optimal PIF-NZSP structure by first creating the integral of the commanded error

$$\dot{\mathbf{y}}_I = \mathbf{y} - \mathbf{y}_m, \quad \dot{\mathbf{y}}_I \in \mathbb{R}^m \quad (34)$$

which upon substituting Eq. (23) becomes

$$\begin{aligned} \dot{\mathbf{y}}_I &= (\mathbf{H}\mathbf{x} + \mathbf{D}\mathbf{u}) - \mathbf{y}_m \\ &= \mathbf{H}\mathbf{x} + \mathbf{D}\mathbf{u} - \mathbf{H}\mathbf{x}^* - \mathbf{D}\mathbf{u}^* \\ &= \mathbf{H}\tilde{\mathbf{x}} + \mathbf{D}\tilde{\mathbf{u}} \end{aligned} \quad (35)$$

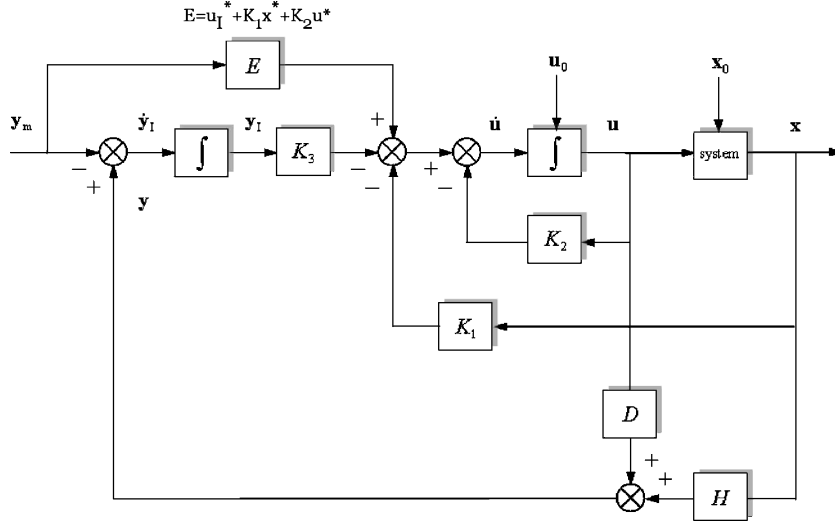


Fig. 7 PIF-NZSP-CRW block diagram.

The augmented state-space system including the control rate states and integrated states is then

$$\dot{\tilde{x}}_I = \begin{bmatrix} \dot{\tilde{x}} \\ \dot{\tilde{u}} \\ \dot{\tilde{y}} + I \end{bmatrix} = \begin{bmatrix} A & B & 0 \\ 0 & 0 & 0 \\ H & D & 0 \end{bmatrix} \begin{bmatrix} \tilde{x} \\ \tilde{u} \\ \tilde{y} + I \end{bmatrix} + \begin{bmatrix} 0 \\ I \\ 0 \end{bmatrix} \tilde{u}_I \quad (36)$$

and the quadratic cost function to be minimized is

$$J = \frac{1}{2} \int_0^\infty (\tilde{x}^T Q_1 \tilde{x} + \tilde{u}^T R \tilde{u} + \tilde{u}_I^T S_{rate} \tilde{u}_I + y_I^T Q_2 y_I) dt \quad (37)$$

where the matrix $Q_1 \in \mathbb{R}^{n \times n}$ weights error states, the matrix $R \in \mathbb{R}^{m \times m}$ weights error controls, the matrix $S_{rate} \in \mathbb{R}^{m \times m}$ weights the control rates, and the matrix $Q_2 \in \mathbb{R}^{p \times p}$ weights the integrated states, with p the number of integrated states. Combining into the standard linear quadratic cost function form results in

$$J = \frac{1}{2} \int_0^\infty \begin{bmatrix} \tilde{x}_I^T \\ \tilde{x}_I^T \end{bmatrix} \begin{bmatrix} Q_1 & 0 & 0 \\ 0 & R & 0 \\ 0 & 0 & Q_2 \end{bmatrix} \begin{bmatrix} \tilde{x}_I \\ \tilde{u}_I \end{bmatrix} dt \quad (38)$$

The minimizing control \tilde{u}_I is obtained from the solution to the matrix algebraic Riccati equation in infinite horizon

$$PA + A^T P - PBR^{-1}B^T P + Q = 0 \quad (39)$$

which results in

$$\tilde{u}_I = -K_1 \tilde{x} - K_2 \tilde{u} - K_3 y_I \quad (40)$$

Rewriting Eq. (40) in terms of the measured state variables produces

$$u_I = (u_I^* + K_1 x^* + K_2 u^*) - K_1 x - K_2 u - K_3 y_I \quad (41)$$

with all * quantities constant, except for u_I^* , which is equal to zero by the definition of steady state. The constants x^* and u^* can be solved for by forming the quad partition matrix

$$\begin{bmatrix} A & B \\ H & D \end{bmatrix}^{-1} = \begin{bmatrix} X_{11} & X_{12} \\ X_{21} & X_{22} \end{bmatrix}, \quad \begin{bmatrix} x^* \\ u^* \end{bmatrix} = \begin{bmatrix} X_{11} & X_{12} \\ X_{21} & X_{22} \end{bmatrix} \begin{bmatrix} 0 \\ y_m \end{bmatrix} \quad (42)$$

and solving for

$$x^* = X_{12} y_m, \quad u^* = X_{22} y_m \quad (43)$$

Upon substituting in Eq. (41), the control policy is

$$u_I = (K_1 X_{12} + K_2 X_{22}) y_m - K_1 x - K_2 u - K_3 y_I \quad (44)$$

Note that this PIF-NZSP control policy requires measurement and feedback of the control positions, in addition to full-state feedback,

in order to be admissible. As with the NZSP, the gains can be determined using any desired technique provided they are stabilizing. In this paper, the gains are designed using linear quadratic methods, thereby providing optimal gains.

UAV Design and Simulation Model

The UAV model used for design and simulation purposes is called UCAV6 (see the Appendix). The UCAV6 simulation is used here because it is representative of the size and dynamical characteristics of a UAV. It is a roughly 60%-scale AV-8B Harrier aircraft (Fig. 1), with the pilot and support devices removed and the mass properties and aerodynamics adjusted accordingly. For the simulations presented here, all thrust-vectoring capability was disabled. The simulation is a nonlinear, non-real-time, six-degree-of-freedom computer code written in Microsoft Visual C++ 5.0. The UCAV6 longitudinal and lateral directional linear models used for both controller synthesis and simulation in this paper were obtained from the UCAV6 nonlinear simulation.¹⁵

Numerical Example

The example will demonstrate the VisNav sensor system and the PIF-NZSP-CRW controller. The GLSDC navigation solution provides the drogue position and attitude estimates directly to the PIF-NZSP-CRW controller. Process and sensor noise obtained from laboratory testing of the VisNav hardware is applied to the VisNav system simulation models. The controller uses full-state feedback, and all gains are designed using the optimal sampled-data technique.¹⁶ The PIF-NZSP-CRW controller is designed by first selecting state and control vectors of

$$x^T = [\delta X \quad \delta Y \quad \delta Z \quad \delta u \quad \delta v \quad \delta w \quad \delta p \quad \delta q \quad \delta r \quad \delta \phi \quad \delta \theta \quad \delta \psi]$$

$$u^T = [\delta ele \quad \delta \% pwr \quad \delta ail \quad \delta rud] \quad (45)$$

where $\delta(\cdot)$ are the perturbations from the steady-state values, and the steady state is assumed as steady level 1-g flight. Here, $\delta X, \delta Y, \delta Z$ are perturbations in the inertial positions; $\delta u, \delta v, \delta w$ are perturbations in the body-axis velocities; $\delta p, \delta q, \delta r$ are perturbations in the body-axis angular velocities; and $\delta \phi, \delta \theta, \delta \psi$ are perturbations in the Euler attitude angles. The control variables δele -elevator, $\delta \% pwr$ -percentage power, δail -aileron, and δrud -rudder are perturbations in the control effectors from the trim values.

The basic NZSP structure permits a number of commanded outputs equal to the number of controls, and so with four controls (elevator, aileron, rudder, throttle) the controller commands the UAV inertial positions to the drogue position (x_d, y_d, z_d), with a specified

yaw attitude angle. The sample period is $T = 0.1$ s for all subsystems in the combined system.

The control objective is to dock the tip position of the refueling probe with a stationary drogue receptacle with an accuracy of ± 2 cm. The initial position of the drogue is arbitrarily selected to be 30 m in front, 30 m above, and 7.5 m to the left of the initial trimmed position of the VisNav equipped UAV. An important requirement is to ensure that the probe engages the drogue with a forward velocity less than 3 m/s, so as to minimize impact damage to the drogue.⁴ The drogue basket is configured with eight LED VisNav beacons. The four outer beacons are located 20 cm from the nozzle in a 36-cm-diam circle. This location corresponds to a typical location where LED lights are currently installed by drogue manufacturers for nighttime refueling operations. The inner four beacons are located near the nozzle itself in a circle with a diameter of 5 cm (Fig. 8). The VisNav PSD sensor is mounted on the UAV, 0.5 m behind the tip of the refueling probe and 13 cm below it.

For this example, the VisNav relative position estimates are obtained from a simulation of the VisNav system that includes calibrations, range effects, corrections caused by optical distortions, and sensor noise. The high-fidelity VisNav sensor system simulation is integrated with the PIF-NZSP-CRW controller, whose feedback measurements are provided by VisNav. The system is simulated for a flight condition of 250 kn true airspeed at 6000-m altitude, for test cases of still air and turbulent air.

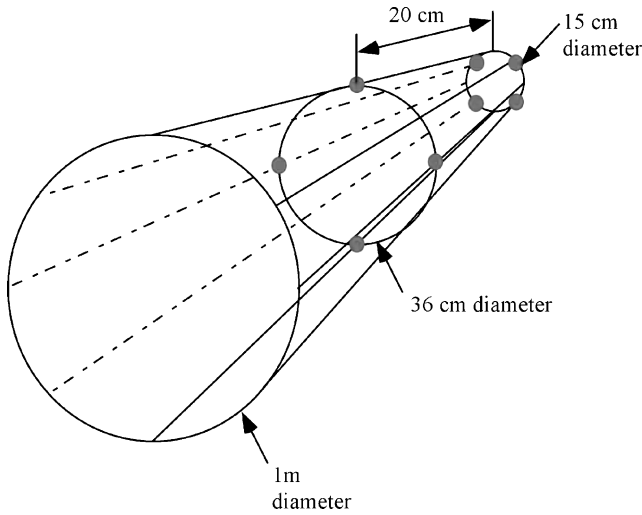


Fig. 8 VisNav LED beacon configuration on drogue basket.

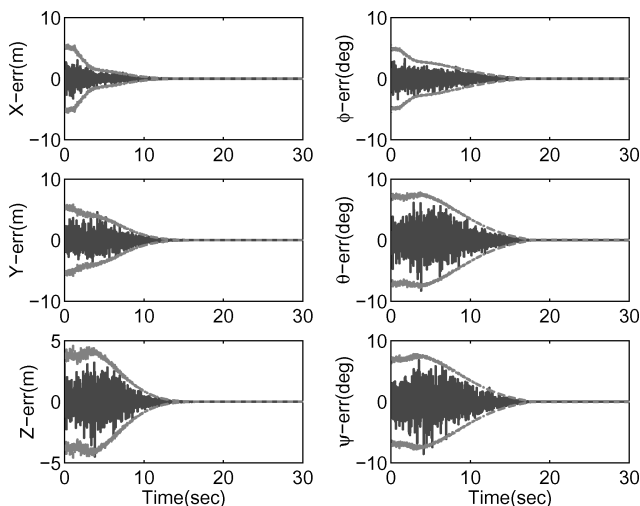


Fig. 9 VisNav 3- σ position and Euler-angle estimation error bounds.

Still Air

For the still-air case, the drogue remains stationary in Y and Z and moves with a constant velocity along the inertial X axis. The three standard deviation estimation errors from VisNav (Fig. 9) are seen to converge well as the probe approaches and then contacts the drogue at time equal to 17 s. Figure 10 shows the trajectory of the tip of the refueling probe, with the receiver aircraft initially maneuvering laterally and vertically to line up with the drogue, and then slowly steering straight toward the probe until contact is made. Figures 11–14 show that the system performs well and meets

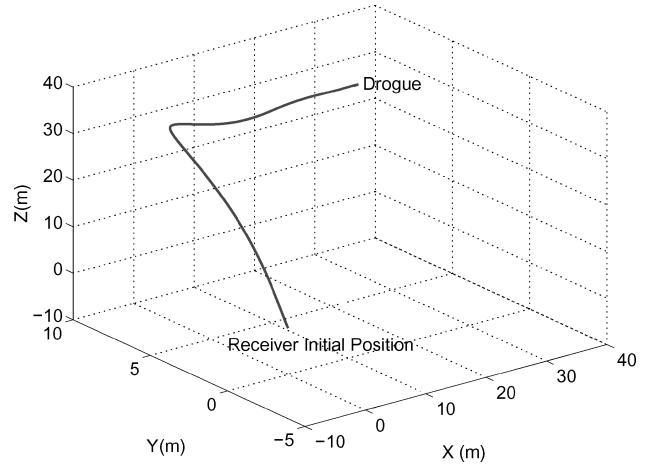


Fig. 10 Probe tip trajectory for simulated docking maneuver.

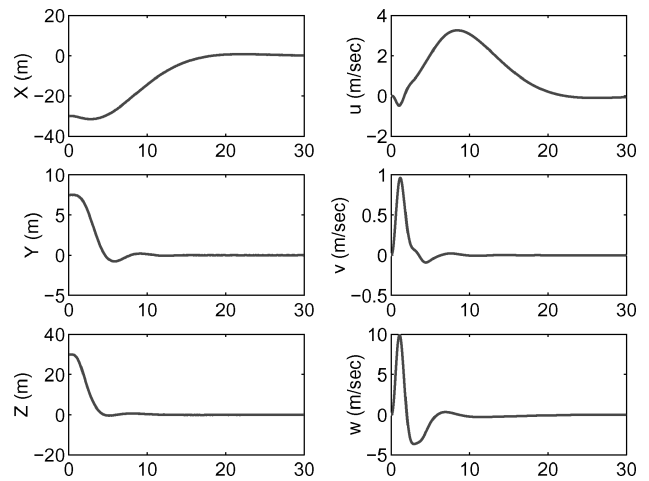


Fig. 11 Probe-drogue relative position errors and velocities.

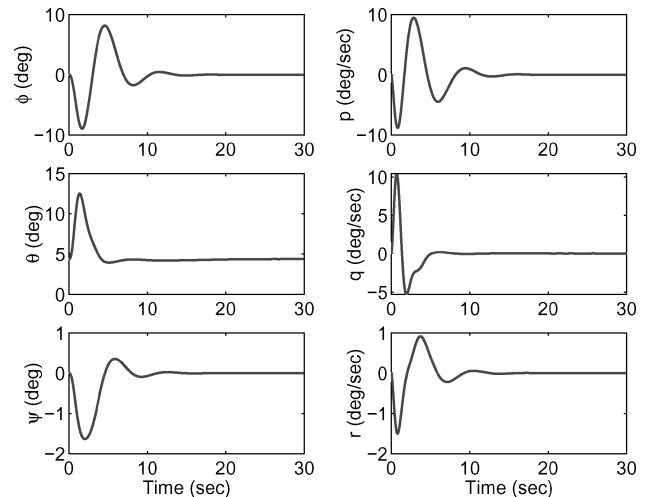


Fig. 12 Probe-drogue relative angular orientation and angular velocities.

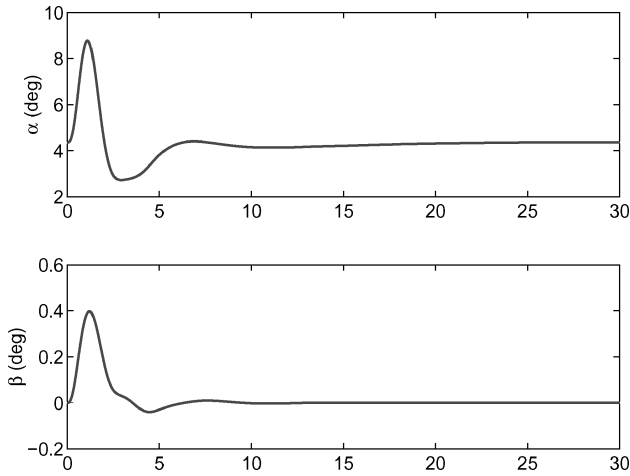


Fig. 13 Aircraft aerodynamic angles.

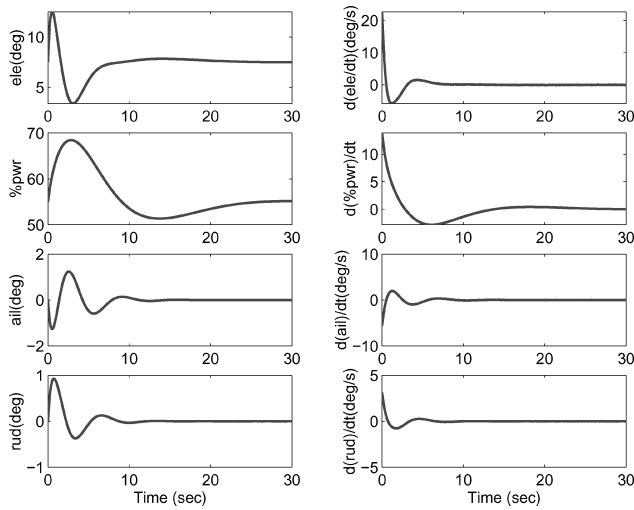
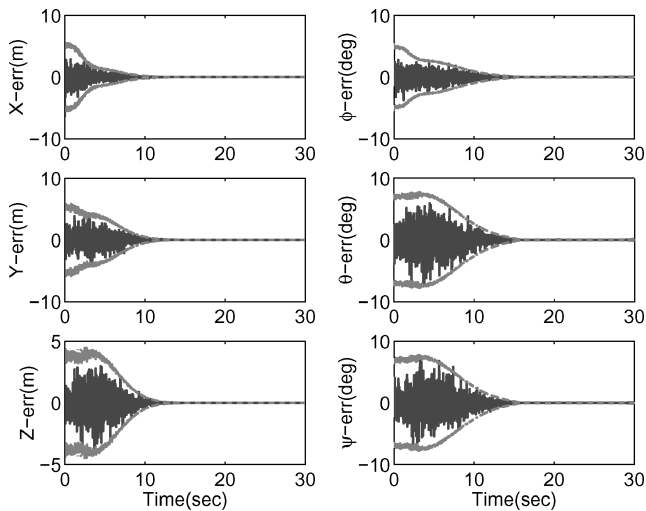


Fig. 14 Control effector positions and rates.

Fig. 15 VisNav 3- σ position and Euler-angle estimation error bounds, with turbulence.

all specifications. The position errors (Fig. 11) converge smoothly and quickly, while the downrange (X) error converges more slowly, to satisfy the maximum docking speed requirement. All angular displacements and rates are small and within bounds (Fig. 12), whereas angle-of-attack and sideslip-angle excursions are small and well damped, as shown in Fig. 13. Figure 14 shows that the control positions and rates are well within acceptable position and rate limits.

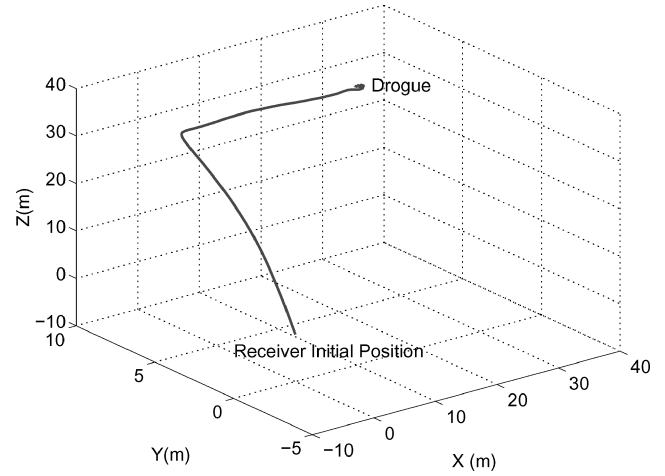


Fig. 16 Probe tip trajectory for simulated docking maneuver.

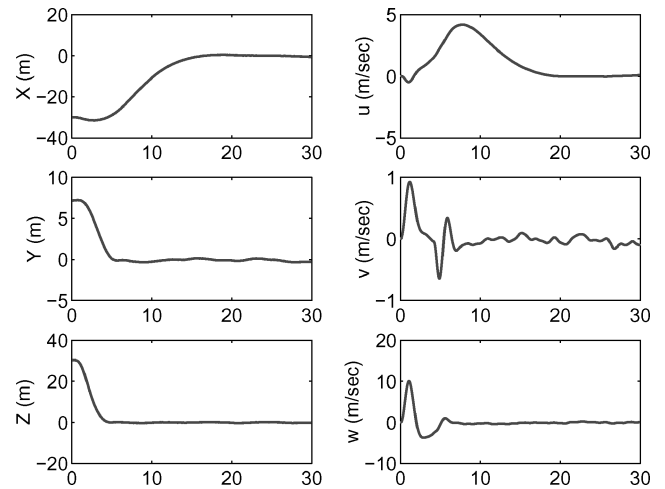


Fig. 17 Probe-drogue relative position errors and velocities.

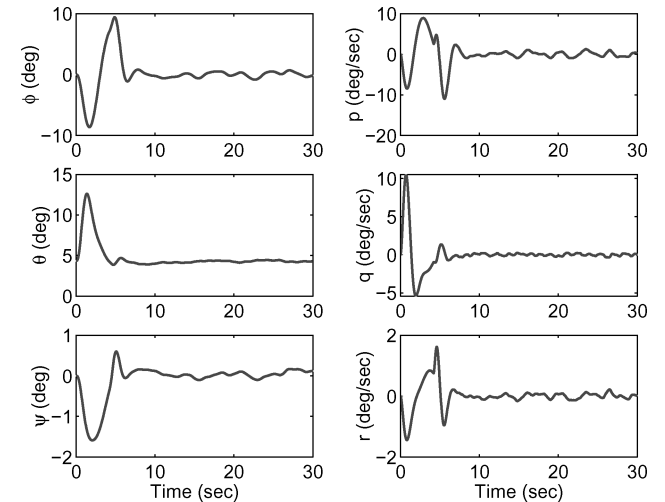


Fig. 18 Probe-drogue relative angular orientation and angular velocities.

Light Turbulence

For this case both the receiver aircraft and the drogue are subjected to light turbulence generated with the Dryden gust model, using a sigma gust value of three. The bandwidth requirements on the controller are less demanding when the probe is farther away from the drogue than when it is very close to the drogue. To track a moving drogue, the controller must respond quickly, and this requires high gains. Conversely, if the high gains are used when the probe is far

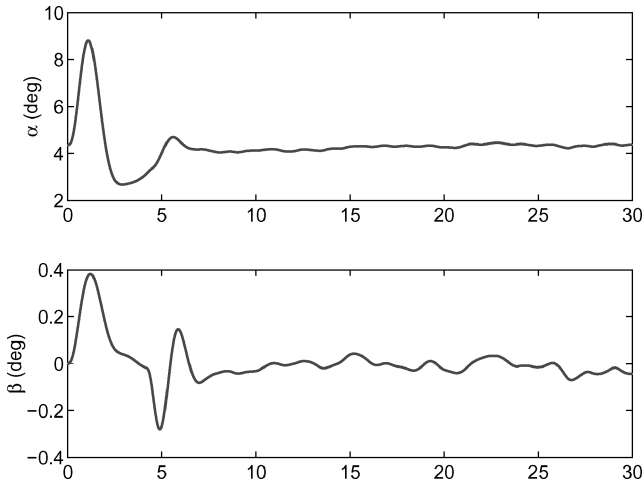


Fig. 19 Aircraft aerodynamic angles.

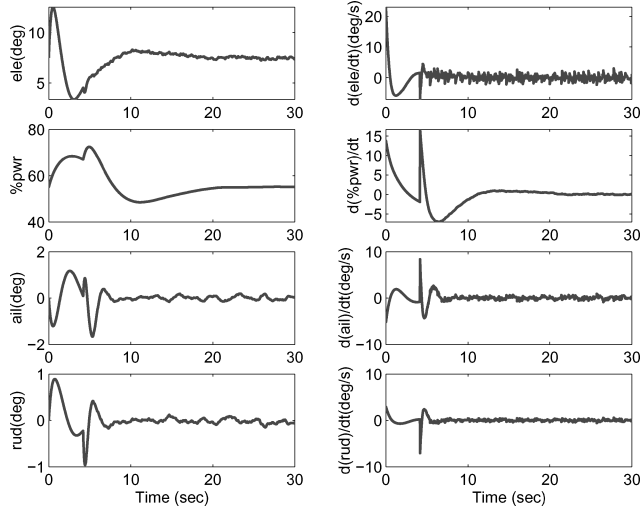


Fig. 20 Control effector positions and rates.

away from the drogue, excessive rates in the states and, in particular, the controls, are generated. Therefore two sets of gains are used for this case. If the position error between the probe and drogue $[\sqrt{(Y^2 + Z^2)}]$ is greater than 1 m, a low gain ($K1$) is used. A higher gain ($K2$) is used otherwise.

Figure 15 shows the three standard deviation estimation errors from VisNav. In spite of the rapid motion of the beacons relative to the sensor, good converge is achieved. Figure 16 shows that the

gain scheduling helps the tip of the probe to track the movements of the drogue in the presence of light turbulence. Note that the small transient in all time histories at $t = 4.2$ s is caused by the switch in control gains from $K1$ to $K2$. The desired low-pass filtering effect of the PIF-NZSP is realized because the probe motions are smoothed and the controls do not experience high rates. Although the probe trajectory lags the drogue trajectory, successful docking is achieved, but not within the tolerance of the docking error specification. However, all other specifications are met, and Figs. 17–20 indicate that the system performs well overall. This result is not unexpected because the basic NZSP controller structure assumes a constant reference, and the reference here is moving. In this work the NZSP controller was only meant to provide a baseline controller to demonstrate the VisNav system. For improved docking performance in the presence of turbulence, a more advanced controller capable of tracking moving references with zero steady-state error is required and forms the subject of follow-on work.

Conclusions

This paper presented the preliminary design of an accurate vision-based sensor system for application to autonomous aerial refueling. The essential features of the navigation sensor and autonomous controller are developed and discussed. The sensor makes use of closed structured light in a way that makes the navigation robust with respect to off-nominal lighting and system performance. The control system utilizes an optimal proportional-integral-filter nonzero set-point control law, which receives relative position measurements derived from a VisNav system of light-emitting-diode beacons, a position-sensing diode sensor, and associated relative navigation algorithms. The system was simulated for the case of docking with a stationary drogue from an initial displacement in longitudinal, lateral, and vertical positions, and also in the presence of turbulence. Results indicate that the system is able to successfully accomplish the autonomous docking task within specifications of docking accuracy, maximum docking velocity, and control effector position, rate, and activity. The gain scheduling and disturbance accommodation properties of the controller in turbulence are judged to be good and provide a basis for optimism as regards to proceeding toward actual implementation. Further investigations are required to extend the controller structure to more effectively track time-varying commands and to evaluate performance with the full suite of additional sensor dynamics and measurement error models applied. It is recommended that these studies be done in parallel with implementation for further laboratory and flight tests.

Appendix: UCAV6 Linear Model

The linear model is obtained by linearizing about steady level flight. The trim values are angle of attack $\alpha_0 = 4.35$ deg, trim velocity $V_0 = 128.7$ m/s, trim elevator deflection $ele_0 = 7.5$ deg, and trim engine power input $pwr_0 = 55\%$. The state vector is

$$x = [\delta X \quad \delta Y \quad \delta Z \quad \delta u \quad \delta v \quad \delta w \quad \delta p \quad \delta q \quad \delta r \quad \delta \phi \quad \delta \theta \quad \delta \psi] \quad (A1)$$

$$A = \begin{bmatrix} 0 & 0 & 0 & 0.99 & 0 & 0.0759 & 0 & 0 & 0 & 0 & -9.77 & 0 \\ 0 & 0 & 0 & 0 & 1 & 0 & 0 & 0 & 0 & -9.77 & 0 & 128.7 \\ 0 & 0 & 0 & -0.07 & 0 & 0.99 & 0 & 0 & 0 & 0 & -127.2 & 0 \\ 0 & 0 & 0 & -0.03 & 0 & 0.16 & 0 & -9.75 & 0 & 0 & -9.75 & 0 \\ 0 & 0 & 0 & 0 & -0.33 & 0 & 9.75 & 0 & -127.4 & 9.75 & 0 & 0 \\ 0 & 0 & 0 & -0.06 & 0 & -1.34 & 0 & 124.8 & 0 & 0 & -0.74 & 0 \\ 0 & 0 & 0 & 0 & -0.02 & 0 & -3.64 & 0 & 1.72 & 0 & 0 & 0 \\ 0 & 0 & 0 & 0 & 0 & -0.07 & 0 & -0.77 & 0 & 0 & 0 & 0 \\ 0 & 0 & 0 & 0 & 0.058 & 0 & -0.21 & 0 & -1.19 & 0 & 0 & 0 \\ 0 & 0 & 0 & 0 & 0 & 0 & 1 & 0 & 0.07 & 0 & 0 & 0 \\ 0 & 0 & 0 & 0 & 0 & 0 & 0 & 1 & 0 & 0 & 0 & 0 \\ 0 & 0 & 0 & 0 & 0 & 0 & 0 & 0 & 1.003 & 0 & 0 & 0 \end{bmatrix} \quad (A2)$$

The control vector is

$$u = [\delta ele \quad \delta \% pwr \quad \delta ail \quad \delta rud] \quad (A3)$$

$$B = \begin{bmatrix} 0 & 0 & 0 & 0 \\ 0 & 0 & 0 & 0 \\ 0 & 0 & 0 & 0 \\ 0.0025 & 0.0780 & 0 & 0 \\ 0 & 0 & -0.0898 & 0.1366 \\ 0.0845 & 0.0697 & 0 & 0 \\ 0 & 0 & 0.5171 & 0.0704 \\ 0.1164 & 0.0143 & 0 & 0 \\ 0 & 0 & 0.0239 & -0.0895 \\ 0 & 0 & 0 & 0 \\ 0 & 0 & 0 & 0 \\ 0 & 0 & 0 & 0 \end{bmatrix} \quad (A4)$$

Acknowledgments

This research is funded by a National Defense Science and Engineering Graduate Fellowship in conjunction with the Army Research Office; by StarVision Technologies, Inc.; by the State of Texas Advanced Technology Program; and by Zonta International Women's Organization. This support is gratefully acknowledged by the authors. The authors also thank Roshawn Bowers for contributions to this paper and the Associate Editor and reviewers for their many insightful comments and suggestions, which improved the paper.

References

- ¹Smith, R. K., "Seventy-Five Years of Inflight Refueling," *Air Force and Museums Program*, U.S. Government Printing Office, Washington, DC, 1998.
- ²Pennington, R. J., "Tankers," *Air and Space Smithsonian*, Vol. 12, No. 4, Nov. 1997, pp. 24–37.
- ³Maiersperger, W. P., "General Design Aspects of Flight Refueling," *Aeronautical Engineering Review*, Vol. 13, No. 3, March 1954, pp. 52–61.
- ⁴Stephenson, J. L., "The Air Refueling Receiver That Does Not Complain," Ph.D. Dissertation, School of Advanced Airpower Studies, Air Univ., Maxwell AFB, AL, June 1998.
- ⁵Andersen, C. M., "Three Degree of Freedom Compliant Motion Control for Robotic Aircraft Refueling," Air Force Inst. of Technology, Afit/gae/eng/90d-01, Wright-Patterson AFB, OH, 13 Dec. 1990.
- ⁶Bennett, R. A., "Brightness Invariant Port Recognition for Robotic Aircraft Refueling," Air Force Inst. of Technology, Afit/ge/eng/90d-04, Wright-Patterson AFB, OH, Dec. 1990.
- ⁷Shipman, R. P., "Visual Servoing for Autonomous Aircraft Refueling," Air Force Institute of Technology, Afit/ge/eng/89d-48, Wright-Patterson AFB, OH, Dec. 1989.
- ⁸Abidi, M. A., and Gonzalez, R. C., "The Use of Multisensor Data for Robotic Applications," *IEEE Transactions on Robotics and Automation*, Vol. 6, No. 2, 1990, pp. 159–177.
- ⁹Lachapelle, G., Sun, H., Cannon, M. E., and Lu, G., "Precise Aircraft-to-Aircraft Positioning Using a Multiple Receiver Configuration," National Technical Meeting, Inst. of Navigation, Jan. 1994.
- ¹⁰Alonso, R., Crassidis, J. L., and Junkins, J. L., "Vision-Based Relative Navigation for Formation Flying of Spacecraft," AIAA Paper 2000-4439, Aug. 2000.
- ¹¹Junkins, J. L., Hughes, D., Wazni, K., and Pariyapong, V., "Vision-Based Navigation for Rendezvous, Docking, and Proximity Operations," *Advances in the Astronautical Sciences*, Vol. 101, 1999, pp. 203–220.
- ¹²Wazni, K. P., "Vision Based Navigation Using Novel Optical Sensors," M.S. Thesis, Aerospace Engineering Dept., Texas A&M University, College Station, TX, Dec. 1999.
- ¹³Schaub, H. P., and Junkins, J. L., *Analytical Mechanics of Space Systems*, AIAA Education Series, AIAA, Reston, VA, 2003, pp. 107–155.
- ¹⁴Gunnam, K., Hughes, D., Junkins, J., and Nasser, K.-N., "A DSP Embedded Optical Navigation System," *Proceedings of the Sixth International Conference on Signal Processing (IC SP '02)*, Vol. 2, Inst. of Electrical and Electronics Engineers, Piscataway, NJ, 2002, pp. 1735–1739.
- ¹⁵Kimmet, J., Valasek, J., and Junkins, J. L., "Autonomous Aerial Refueling Utilizing a Vision Based Navigation System," AIAA Paper 2002-4469, Aug. 2002.
- ¹⁶Dorato, P., "Optimal Linear Regulators: The Discrete-Time Case," *IEEE Transactions on Automatic Control*, Vol. AC-16, No. 6, 1971, pp. 613–620.